ε−ζ transition in solid oxygen

S. F. Elatresh [*]

Physics Department and Interdisciplinary Research Center for Intelligent Secure Systems,
[King Fahd University of Petroleum and Minerals](), Dhahran 31261, Saudi Arabia

V. Askarpour

Department of Physics, [Dalhousie University](), Halifax, Canada NS B3H 3J5

S. A. Bonev [†]

[Lawrence Livermore National Laboratory](), Livermore, California 94550, USA

The structure of solid oxygen has been studied at pressures from 50 to 140 GPa using static structure search methods and molecular dynamics simulations with density functional theory and a hybrid exchange functional. Several crystalline structures with space group symmetries $Pnma$, $P\,2_1/m$, Pm, and $P\,6_3/mmc$ have been identified as candidates for the ζ phase of oxygen at 0 K. Within the hybrid exchange functional framework and at 300 K temperature, Pm is shown to be energetically most favorable above 111 GPa. A comparison with experimental x-ray diffraction, spectroscopic, and superconductivity measurements is provided for all competing structures.

I. INTRODUCTION

Oxygen is, in many ways, a unique element: fundamental, abundantly available on Earth, and the only known diatomic molecule that carries a magnetic moment [1]. Its phase diagram is a good example of the abundance of interesting physical properties, which emerge under compression. Multiple phases have been discovered at low pressure, including the γ, α, β, δ, η, and ε phases [1–16], which are molecular and the structural differences among them are in the relative arrangements of the O_2 molecules. At room temperature, solid oxygen exists in the nonmagnetic [17] insulating ε phase between 10 GPa and 96 GPa [1,18], above which it undergoes an insulator-to-metal transformation to the ζ phase [3]. The latter transition appears to be gradual and completed by 110 GPa [19].

The ε phase, which remains stable across a wide range of pressures, has attracted a lot of interest, encompassing both theoretical investigations [20–30] and experimental examinations employing x-ray diffraction [3,19,31,32] and spectroscopic measurements [33–37]. Powder [3,18] and single-crystal [19] x-ray diffraction studies indicated that the ε phase has a monoclinic $C\,2/m$ symmetry with a primitive cell with a single O_8 cluster consisting of four molecules. A theoretical GW analysis of the ε phase reported that the structural transformation to ε is accompanied by an insulator-metal transition at 51.7 GPa [38] while a later GW study suggested a transition pressure of about 100 GPa [39].

Although the structure of the ε phase is experimentally known [1,18,20], that of the ζ phase remains a subject of continued debate. Raman measurements [40] demonstrated that the ζ phase is molecular with at least four O_2 pairs in the primitive unit cell, while conductivity data [13] suggested superconductivity below 0.6 K. While Raman and single-crystal x-ray diffraction experiments [19,40] seemed to imply that the ε and ζ phases are not isostructural, powder x-ray diffraction [3] and more recent single-crystal x-ray and Raman studies [41] proposed the structure of ζ-O_2 to be monoclinic with symmetry $C\,2/m$ [hereafter referred to as ζ-$C\,2/m$ to distinguish it from ε-$C\,2/m$, which we will refer to as ε-(O_8)]. The structural refinement from the latter measurements relied on *ab initio* crystal structure predictions [42] performed within the generalized gradient approximation (GGA) to density functional theory (DFT). This approach proposed the structure of ζ-O_2 to be $C\,2/m$. However, several discrepancies exist between the theoretical predictions and experimental data.

We recall that the lowest-enthalpy structure for the ε phase was initially predicted to be $Cmcm$ and not the experimentally determined O_8 (ε-$C\,2/m$). In addition, DFT calculations within GGA initially suggested that the ε-ζ transition occurs at approximately 40 GPa, in contrast to the experimental value of 96 GPa. These discrepancies were recently resolved by independent theoretical studies [27,28,43,44] where the researchers emphasized the significance of employing accurate exchange-correlation (XC) functionals beyond the GGA.

The present study is focused on the ε-ζ transition and determining the structure of the ζ phase. Several new candidate structures for the ζ phase are found using the universal structure predictor evolutionary xtallography (USPEX) code [45–50]. In light of the the recent studies [27,28,43,44] elucidating the importance of using accurate exchange-correlation

---

[*]Contact author: sabri.elatresh@kfupm.edu.sa
[†]Contact author: bonev@llnl.gov

functionals, we have performed hybrid exchange calculations within the Heyd-Scuseria-Ernzerhof approximation (HSE06) [51]. Based on them, a HSE06-modified phase diagram is proposed. Furthermore, molecular dynamics simulations of the candidate structures are performed and their HSE06-corrected Gibbs free energies are computed for a final relative stability ordering of the candidate structures.

II. COMPUTATIONAL DETAILS

Electronic structure calculations and structural relaxations were performed within DFT using the Vienna *ab initio* simulation package (VASP) [52,53]. The generalized gradient approximation (GGA) along with projector augmented wave (PAW) Perdew-Burke-Ernzerhof (PBE) pseudopotential in which the $2s^2 2p^4$ states were treated as valence states with a core radius of 1.1 a.u. was employed [54,55]. The geometry was optimized using the conjugate gradient algorithm. The Brillouin zone (BZ) **k**-point sampling was performed with the Monkhorst-Pack scheme [56]. The electronic density-of-states (DOS) was calculated on a $20 \times 20 \times 20$ grid in the BZ by the tetrahedron method with Blöchl corrections [57]. Phonon calculations and Raman modes were calculated by density functional perturbation theory (DFPT) [58] as implemented in the ABINIT package [59]. The phonon band structure and density of states (Figs. S12 and S13 [60]) were computed using a $5 \times 5 \times 5$ **q**-point phonon grid to achieve convergence of the dynamical matrices.

Search for new structures were conducted for 16 and 24 atoms at 35 GPa and 150 GPa using the USPEX code [45–50]. In each case, starting from an initial population of 50 random structures, variable-cell relaxation was performed by VASP using a cutoff energy of 800 eV, a $4 \times 4 \times 4$ Monkhorst-Pack grid, and Methfessel-Paxton smearing [61] with a width of 0.1 eV. In addition to several of the lowest-enthalpy structures that automatically moved on to the next generation, 70% of each generation was used to create the next generation by hereditary and mutation. After over 30 generations, the lowest-enthalpy structures (Fig. 1) were further relaxed with an energy cutoff of 1000 eV, a denser, $16 \times 16 \times 16$, BZ sampling grid, and force convergence requirement of 1 meV/Å. Based on convergence tests, these parameters were sufficient to converge the total PBE energies to better than 1 meV/atom.

It is well known that GGA (DFT) underestimates the electronic band gap. Therefore, the HSE06 functional [51] was employed to describe the molecular and electronic properties of solid oxygen. The electron correlation interaction and the long-range part of the exchange interaction were maintained at the PBE level while 25% of Hartree-Fock exact exchange and 75% of the PBE exchange were combined to form the short-range part of the electron-electron exchange interaction. To carry out the demanding HSE06 calculations within a reasonable time, the number of *k* points were lowered [see Fig. 2(b) caption and legend], which introduced an estimated error of 2 meV/atom in the calculated energy values.

The space groups of the new structures were identified with the FINDSYM code [62]. Powder x-ray diffraction patterns were simulated by PowderCell [63]. Using VASP, constant volume molecular dynamics simulations were performed on $P 2_1/m$, *Pnma*, *Pm*, ζ-$C 2/m$, and $P 6_3/mmc$ with
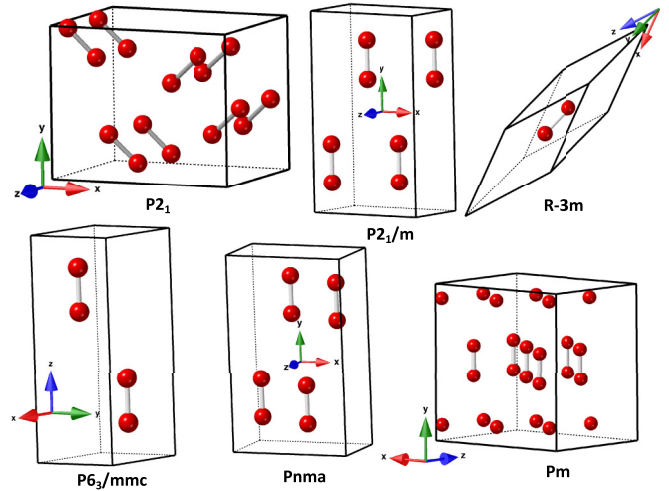

FIG. 1. Candidate crystal structures for solid oxygen at 90 GPa based on static, 0 K, DFT-PBE searches. Shown are the newly found $P2_1$, $P2_1/m$, *R*-3*m*, $P6_3/mmc$, *Pnma*, and *Pm* structures.

PBE pseudopotential and Nosé-Hoover [64,65] thermostat at ~ 116 GPa and ~ 140 GPa at 300 K. The simulation supercells contained 192 atoms for *Pm* with Γ-point sampling and 64 atoms for the other four structures with $2 \times 2 \times 2$ BZ sampling grids. In addition, a supercell of 48 atoms for *Pm* with a $2 \times 2 \times 2$ BZ grid was included. A cutoff energy of 1000 eV and an integration time step of 0.75 fs were used.

III. RESULTS AND DISCUSSION

Note that theoretical generation of the ε-O_8 structure above 50 GPa using the PAW method implemented in VASP is impossible, as the structure spontaneously converts to the metallic ζ-$C 2/m$ [42]. In the present work, ε-O_8 between 30 and 140 GPa is constructed by restricting the electronic occupancies so that the lowest 24 electronic bands remain occupied, thus ensuring that ε-O_8 remains a semiconductor. We have confirmed that the HSE06-relaxed ε-O_8 remains a semiconductor up to ~ 107 GPa at 0 K (see plots of the electron bands structure computed within PBE and HSE in the Supplemental Material, Fig. S1 (a) and (b) [60]). At finite temperature, band broadening due to the atomic motion should lead to gap closure at lower pressure, in better agreement with the experimental value of 96 GPa [3] measured at room temperature.

In addition to the previously suggested $C 2/m$ and $C 2/c$ candidate structures for the ζ phase [42], our structure searches yield several new candidates, namely, R -3m, $P 6_3/mmc$, *Cmcm*, $P 2_1$, *Pnma*, $P 2_1/m$, and *Pm* (Fig. 1). Their lattice parameters are reported in Table I in the Supplemental Material. The first three structures are unlikely candidates for the ζ phase because their primitive cells have bases of only two and four atoms, which are insufficient to account for the measured Raman mode mupltiplicities [40]. The remaining structures consist of 16, 8, 8, and 24 atoms, respectively.

Figure 2(a) compares the PBE enthalpies of the generated phases of oxygen with USPEX. As noted by Ma *et al.* [42], $C 2/m$ is the dominant structure at the pressures
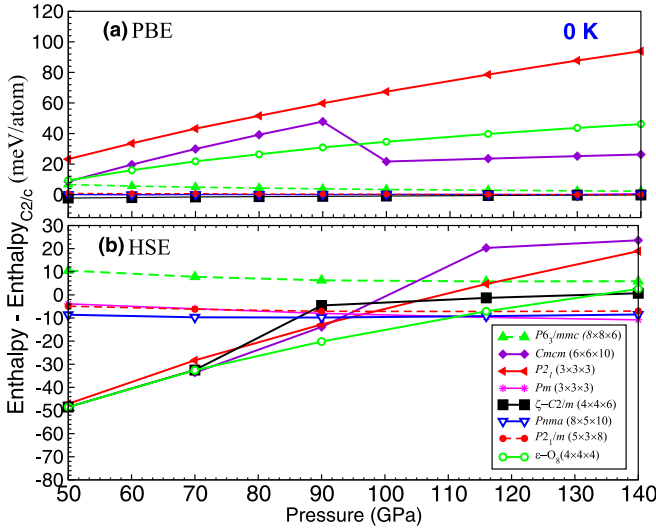
FIG. 2. Enthalpies of various structures of oxygen relative to the $C\,2/c$ phase relaxed within (a) PBE and (b) HSE06. In the HSE06 calculations, the **k**-point meshes were $8 \times 8 \times 4$ for $C\,2/c$ and as specified in the legend for the remaining structures.

FIG. 3. HSE06-corrected Gibbs free energy difference relative to the $Pnma$ structure at 300 K.

considered here. However, the enthalpy differences between $Pnma$, $P\,2_1/m$, Pm, and $C\,2/c$ are less than 1 meV/atom. The discontinuity in the enthalpy curve of $Cmcm$ is due to a transition to another structure with the same space group, $Cmcm$, above 90 GPa, as seen in the discontinuity of its lattice parameters at this pressure (see Fig. S2 [60]). All these structures are molecular with an O_2 bond distance of about 1.18 Å, and the differences among them are in the relative arrangement of the molecules (see Figs. S3 to S8 for neighbor distance distribution analysis [60]). Furthermore, all candidate structures for the ζ phase are metallic, which is consistent with the experimental observation [3]. Their electronic properties were evaluated at 0 K (see electronic DOS at 140 GPa in Fig. S9 [60]) and for the $P\,2_1/m$, $Pnma$, Pm, and ζ-$C\,2/m$ structures at 300 K and ~116 GPa. The latter was done by calculating average DOS over molecular dynamics simulations (see below) and employing the HSE06 functional at the electronic level. In all cases, the electronic band gap is closed.

After inclusion of the HSE06 hybrid functional in the geometrical optimization, the relative stability of the candidate structures changes significantly. The modified enthalpy curves are shown in Fig. 2(b). In contrast to the PBE result, ε-O_8 is the energetically preferred structure below 111 GPa, while $Pnma$ and Pm are the lowest-enthalpy structures above this pressure. Within HSE06, the enthalpy of ζ-$C\,2/m$ becomes about 9 meV/atom higher than that of both $Pnma$ or Pm at 116 GPa. These are small enthalpy differences, which can be overcome by the phonon free energies even at room temperature.

To determine thermodynamic stability at finite temperature, we have performed constant-volume first principles molecular dynamics (FPMD) simulations at densities corresponding to pressures of about 116 and 140 GPa and temperature of 300 K for $P\,2_1/m$, $Pnma$, Pm, $P\,6_3/mmc$, and ζ-$C\,2/m$. Equilibrium was established within the first 2 ps of the simulations, and data was collected in the following 5 ps.
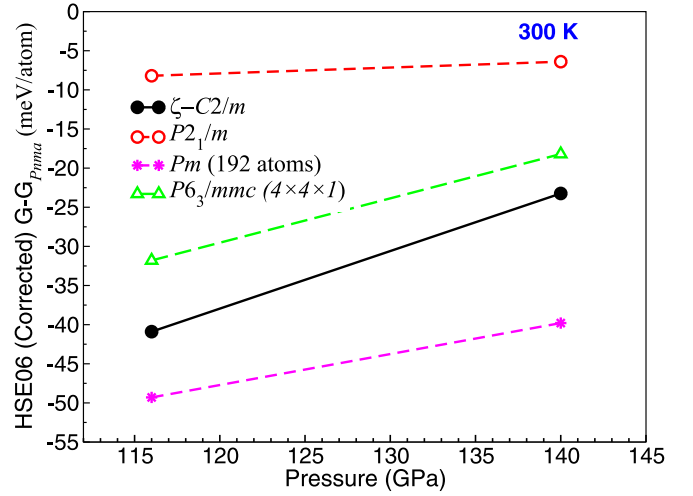
The enthalpies of all structures, $H = U + PV$, were obtained directly from the FPMD at the level of DFT-PBE, with U and P as statistical averages of the instantaneous energy and pressure. HSE06 corrections to the enthalpy were then made as $\Delta H_{HSE} = \langle E_{HSE} - E_{PBE} \rangle_{PBE}$, where E_{HSE} and E_{PBE} are HSE and PBE energies, respectively, of atomic configurations taken from the FPMD trajectories, and $\langle \cdots \rangle_{PBE}$ indicates statistical average within the PBE-FPMD ensemble. The quantum ion dynamics contributions to the energies cancel out and do not alter the relative stability of the structures. To obtain the Gibbs free energy, $G = H - TS$, the entropies, S, of all structures were computed by integrating their vibrational density of states (VDOS) assuming a harmonic partition function. The VDOS were obtained by Fourier transforming velocity autocorrelation functions from the FPMD trajectories. The relative HSE-corrected Gibbs free energies of the relevant structures are shown in Fig. 3.

Note that the differences among the Gibbs free energies of the candidate structures are more significant than the 0 K enthalpy differences, which allows us to draw stronger conclusions for their stability. Based on the HSE06-corrected Gibbs free energy data presented in Fig. 3, the energetically most favorable structure in the stability region of the ζ phase is Pm. The transition pressure from ε-O_8 to Pm can be estimated to be around 100 GPa.

The Pm structure has a near hexagonal close packed ($P\,6_3/mmc$) symmetry with a 24-atom unit cell with oxygen atoms at the 2c Wyckoff positions. Figure 4 shows two neighboring basal planes of Pm at ~ 116 GPa. Here a layer is shown in blue and the next one in red; the layers have $ABAB$ stacking. To confirm the mechanical stability of Pm, we have computed its phonon band structure and density of states (see Figs. S12 and S13 [60]), which show no imaginary modes.

In what follows, we compare properties of the energetically most competitive structures to experimental measurements of ζ-oxygen phase.

Simulated powder x-ray diffraction patterns for the HSE06-relaxed $P\,2_1/m$, $Pnma$, Pm, ζ-$C\,2/m$, and $P\,6_3/mmc$ at 116 GPa are shown in Fig. 5, along with the x-ray peak
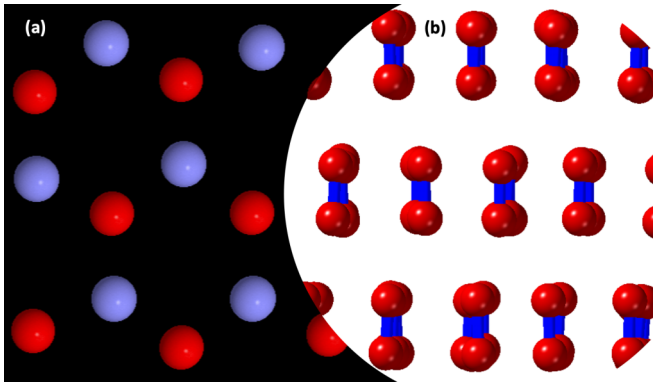
FIG. 4. View of the *Pm* structure at 116 GPa and 300 K (a) a long the O_2 bond and (b) side view.
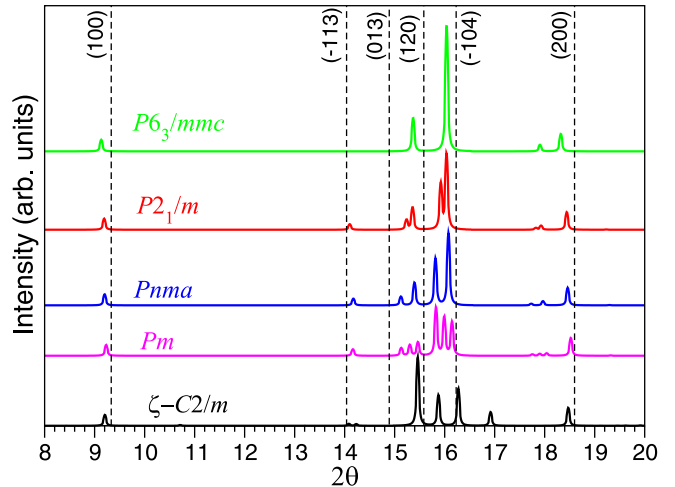

FIG. 5. Simulated powder x-ray diffraction for HSE06-relaxed structures at 116 GPa. Experimental peaks are shown with dashed black lines [3]. More recent experimental measurements at 140 GPa report similar diffraction pattern [67].

positions (dashed black lines) from experimental measurements obtained at the same pressure [3]. The patterns for $P 2_1/m$ and *Pnma* are almost identical to each other, as these two structures are nearly isostructural. Previous analysis of x-ray data [3,41] has suggested that the structure of the ζ phase is monoclinic $C 2/m$. Additionally, it has been suggested that the experimental peak at 14.9° belongs to the ε phase, as the ζ and ε coexist from 96 to 128 GPa. However, we see here that all five structures show a reasonable agreement with the experimental data, though none of them matches the data perfectly. The measured [3] x-ray peaks between 14° and 16° are rather broad and overlapping. One can argue that there are multiple peaks in this region, which are difficult to separate, in which case *Pm* provides the best agreement with the data.

Metallic oxygen in the ζ phase has been found to be superconducting with a measured [13] critical temperature (T_c) of 0.6 K. Here we have estimated the values of T_c for the HSE06-relaxed $P 2_1/m$, *Pnma*, *Pm*, ζ-$C 2/m$, and $P 6_3/mmc$ structures at 116 GPa. They were calculated using the ABINIT [59] package, with the McMillan's formula [66] and an average electron-electron Coulomb interaction length of 0.136. The T_c estimates for the above phases are 30, 1.6, 6.2, 0.02, and 9.4 K, respectively. The computed T_c for *Pnma* (1.6 K) and ζ-$C 2/m$ (0.02 K) are closest to the experimental value. However, except for $P 2_1/m$, the differences are small and the McMillan formula estimate is insufficient to discriminate among them, while more accurate superconducting calculations are beyond the scope of this paper.

Raman measurements on the ζ phase [40,67] indicate the presence of (at least) seven optical modes. $P 6_3/mmc$ has only three Raman active modes. *Pnma* and ζ-$C 2/m$ cannot account for all Raman modes either (see Fig. S10 in the Supplemental Material [60]). Finally, *Pm* has 69 optical modes, which are both infrared and Raman active. It accounts for all measured Raman peaks, but exhibits extra modes as well. A possible explanation for this seeming discrepancy is that many of the optical modes are too weak to observe experimentally. Similarly to the x-ray data, the Raman peaks in the 400–900 cm^{-1} range are broad and overlapping. This is the frequency region where most of the extra *Pm* modes are. Thus, another possibility is that individual modes are hard to identify from the available experimental data.

VI. CONCLUSIONS

In summary, we have performed first-principles crystal structure searches identifying several new candidate structures for the ζ phase of oxygen. DFT calculations with a hybrid exchange functional (HSE06), which correctly predicts the ε phase and the insulator-to-metal transition of oxygen at 0 K, significantly alter the relative stability of these structures compared to DFT-GGA. Even bigger effect has the inclusion of finite-temperature effects. The final energetic ordering is established from Gibbs free energies calculated using molecular dynamics simulations performed at room temperature and with HSE06 corrections at the level of thermodynamic perturbation theory.

Based on this analysis, the structure with lowest free energy in the stability region of the ζ phase of oxygen is a nearly hexagonal close-packed structure with *Pm* symmetry and a 24 atom-unit cell. Comparison with available experimental data shows a reasonable agreement with x-ray and Raman measurements—similar to that of the previously proposed $C 2/m$ structure, but not perfect. During the peer review process of this article, new experimental measurements were published by Dalladay-Simpson *et al.* [67]. However, despite the higher quality Raman data and eliminating issues stemming from the presence of a mixed-state phase, the agreement with any of the theoretically predicted structures remains imperfect. Given that experimental interpretations have relied on theoretical structure predictions, we consider this study a valuable contribution toward eventually determining the equilibrium structure of ζ oxygen conclusively, for example, once higher quality x-ray measurements become available.

---

[1] L. F. Lundegaard, G. Weck, M. I. McMahon, S. Desgreniers, and P. Loubeyre, Observation of an O_8 molecular lattice in the ε phase of solid oxygen, Nature (London) **443**, 201 (2006).

[2] Yu. A. Freiman, H. J. Jodl, and Y. Crespo, Solid oxygen revisited, Phys. Rep. **743**, 1 (2018).

[3] Y. Akahama, H. Kawamura, D. Häusermann, M. Hanfland, and O. Shimomura, New high-pressure structural transition of oxygen at 96 GPa associated with metallization in a molecular solid, Phys. Rev. Lett. **74**, 4690 (1995).

[4] Yu. A. Freiman and H. J. Jodl, Solid oxygen, Phys. Rep. **401**, 1 (2004).

[5] E. M. Hörl, Structure and structure imperfections of solid β-oxygen, Acta Crystallogr. **15**, 845 (1962).

[6] R. LeSar and R. D. Etters, Character of the α -β phase transition in solid oxygen, Phys. Rev. B **37**, 5364 (1988).

[7] L. F. Lundegaard, C. Guillaume, M. I. McMahon, E. Gregoryanz, and M. Merlini, On the structure of high-pressure high-temperature η-O_2, J. Chem. Phys. **130**, 164516 (2009).

[8] R. J. Meier and R. B. Helmholdt, Neutron-diffraction study of α- and β-oxygen, Phys. Rev. B **29**, 1387 (1984).

[9] D. Schiferl, D. T. Cromer, L. A. Schwalbe, and R. L. Mills, Structure of 'orange' $^{18}O_2$ at 9.6 GPa and 297 K, Acta Cryst. Sec. B **39**, 153 (1983).

[10] F. A. Gorelli, M. Santoro, L. Ulivi, and M. Hanfland, Crystal structure of solid oxygen at high pressure and low temperature, Phys. Rev. B **65**, 172106 (2002).

[11] I. N. Goncharenko, O. L. Makarova, and L. Ulivi, Direct determination of the magnetic structure of the delta phase of oxygen, Phys. Rev. Lett. **93**, 055502 (2004).

[12] S. Desgreniers, Y. K. Vohra, and A. L. Ruoff, Optical response of very high density solid oxygen to 132 GPa, J. Phys. Chem. **94**, 1117 (1990).

[13] K. Shimizu, K. Suhara, M. Ikumo, M. I. Eremets, and K. Amaya, Superconductivity in oxygen, Nature (London) **393**, 767 (1998).

[14] L. Zhu, Z. Wang, Y. Wang, G. Zou, H.-K. Mao, and Y. Ma, Spiral chain O_4 form of dense oxygen, Proc. Natl. Acad. Sci. USA **109**, 751 (2012).

[15] T. Nomura, Y. H. Matsuda, S. Takeyama, A. Matsuo, K. Kindo, J. L. Her, and T. C. Kobayashi, Novel phase of solid oxygen induced by ultrahigh magnetic fields, Phys. Rev. Lett. **112**, 247201 (2014).

[16] B. Militzer, F. Gygi, and G. Galli, Structure and bonding of dense liquid oxygen from first principles simulations, Phys. Rev. Lett. **91**, 265503 (2003).

[17] M. Chavez, D.-U. Hwang, A. Amann, H. G. E. Hentschel, and S. Boccaletti, Synchronization is enhanced in weighted complex networks, Phys. Rev. Lett. **94**, 218701 (2005).

[18] H. Fujihisa, Y. Akahama, H. Kawamura, Y. Ohishi, O. Shimomura, H. Yamawaki, M. Sakashita, Y. Gotoh, S. Takeya, and K. Honda, O_8 cluster structure of the epsilon phase of solid oxygen, Phys. Rev. Lett. **97**, 085503 (2006).

[19] G. Weck, P. Loubeyre, and R. LeToullec, Observation of structural transformations in metal oxygen, Phys. Rev. Lett. **88**, 035504 (2002).

[20] Y. Meng, P. J. Eng, J. S. Tse, D. M. Shaw, M. Y. Hu, J. Shu, S. A. Gramsch, C.-C. Kao, R. J. Hemley, and H.-K. Mao, Inelastic x-ray scattering of dense solid oxygen: Evidence for intermolecular bonding, Proc. Natl. Acad. Sci. USA **105**, 11640 (2008).

[21] S. Serra, G. Chiarotti, S. Scandolo, and E. Tosatti, Pressure-induced magnetic collapse and metallization of molecular oxygen: The ζ- O_2 phase, Phys. Rev. Lett. **80**, 5160 (1998).

[22] R. Gebauer, S. Serra, G. L. Chiarotti, S. Scandolo, S. Baroni, and E. Tosatti, Noncolinear spin polarization from frustrated antiferromagnetism: A possible scenario for molecular oxygen at high pressure, Phys. Rev. B **61**, 6145 (2000).

[23] J. B. Neaton and N. W. Ashcroft, Low-energy linear structures in dense oxygen: Implications for the ϵ phase, Phys. Rev. Lett. **88**, 205503 (2002).

[24] S. Elatresh, Lithium and oxygen under high pressure: Finite-T phase stability and melting, Ph.D. thesis, Dalhousie University, 2015.

[25] S. Elatresh and S. Bonev, Stability of solid oxygen at high pressure, *Proceedings of the 18th Biennial International Conference of the APS Topical Group on Shock Compression of Condensed Matter* (Seattle, Washington, 2013).

[26] L. T. Anh, M. Wada, H. Fukui, T. Kawatsu, and T. Iitaka, First-principles calculations of the epsilon phase of solid oxygen, Sci. Rep. **9**, 8731 (2019).

[27] A. J. Ochoa-Calle, C. M. Zicovich-Wilson, R. Hernández-Lamoneda, and A. Ramírez-Solís, Understanding the ϵ and ζ high-pressure solid phases of oxygen. systematic periodic density functional theory studies using localized atomic basis, J. Chem. Theory Comput. **11**, 1195 (2015).

[28] A. J. Ochoa-Calle, C. M. Zicovich-Wilson, and A. Ramírez-Solís, Solid oxygen ζ phase and its transition from ε phase at extremely high pressure: A first-principles analysis, Phys. Rev. B **92**, 085148 (2015).

[29] A.J. Ochoa-Calle, C.M. Zicovich-Wilson, and A. Ramírez-Solís, On the raman and infrared vibrational spectra of the ε and ζ phases of oxygen. systematic dft studies with localized basis sets, Chem. Phys. Lett. **638**, 82 (2015).

[30] A. Ramírez-Solís, C. M. Zicovich-Wilson, R Hernandez-Lamoneda, and A. J. Ochoa-Calle, Antiferromagnetic vs. non-magnetic ε phase of solid oxygen. periodic density functional theory studies using a localized atomic basis set and the role of exact exchange, Phys. Chem. Chem. Phys. **19**, 2826 (2017).

[31] S. W. Johnson, M. Nicol, and D. Schiferl, Algorithm for sorting diffraction data from a sample consisting of several crystals enclosed in a sample environment apparatus, J. Appl. Crystallogr. **26**, 320 (1993).

[32] H. Fukui, L. T. Anh, M. Wada, N. Hiraoka, T. Iitaka, N. Hirao, Y. Akahama, and T. Irifune, Electronic structure of dense solid oxygen from insulator to metal investigated with

x-ray raman scattering, Proc. Natl. Acad. Sci. USA **116**, 21385 (2019).

[33] Y. Akahama and H. Kawamura, High-pressure raman spectroscopy of solid oxygen, Phys. Rev. B **54**, R15602 (1996).

[34] F. A. Gorelli, L. Ulivi, M. Santoro, and R. Bini, The ϵ phase of solid oxygen: Evidence of an O_4 molecule lattice, Phys. Rev. Lett. **83**, 4093 (1999).

[35] Y. Akahama and H. Kawamura, High-pressure infrared spectroscopy of solid oxygen, Phys. Rev. B **61**, 8801 (2000).

[36] S. F. Agnew, B. I. Swanson, and L. H. Jones, Extended interactions in the ε phase of oxygen, J. Chem. Phys. **86**, 5239 (1987).

[37] Y. Akahama, H. Fujihisa, N. Hirao, and Y. Ohishi, Jpn. J. Appl. Phys. **58**, 095502 (2019).

[38] D. Y. Kim, S. Lebègue, C. M. Araújo, B. Arnaud, M. Alouani, and R. Ahuja, Structurally induced insulator-metal transition in solid oxygen: A quasiparticle investigation, Phys. Rev. B **77**, 092104 (2008).

[39] J. S. Tse, D. D. Klug, Y. Yao, and S. Desgreniers, Electronic structure of ε-oxygen at high pressure: GW calculations, Phys. Rev. B **78**, 132101 (2008).

[40] A. F. Goncharov, E. Gregoryanz, R. J. Hemley, and H.-K. Mao, Molecular character of the metallic high-pressure phase of oxygen, Phys. Rev. B **68**, 100102 (2003).

[41] G. Weck, S. Desgreniers, P. Loubeyre, and M. Mezouar, Single-crystal structural characterization of the metallic phase of oxygen, Phys. Rev. Lett. **102**, 255503 (2009).

[42] Y. Ma, A. R. Oganov, and C. W. Glass, Structure of the metallic ζ -phase of oxygen and isosymmetric nature of the ε -ζ phase transition: *Ab initio* simulations, Phys. Rev. B **76**, 064101 (2007).

[43] S. F. Elatresh and S. A. Bonev, Stability and metallization of solid oxygen at high pressure, Phys. Chem. Chem. Phys. **22**, 12577 (2020).

[44] A. Ramírez-Solís, A. J. Ochoa-Calle, and R. Hernández-Lamoneda, Core excitations of the solid oxygen ε phase: periodic hybrid density functional theory studies with localized atomic basis, Theor. Chem. Acc. **137**, 32 (2018).

[45] A. R. Oganov and C. W. Glass, Crystal structure prediction using *ab initio* evolutionary techniques: Principles and applications, J. Chem. Phys. **124**, 244704 (2006).

[46] C. W. Glass, A. R. Oganov, and N. Hansen, Uspex–evolutionary crystal structure prediction, Comput. Phys. Commun. **175**, 713 (2006).

[47] A. R. Oganov, C. W. Glass, and S. Ono, High-pressure phases of $CaCo_3$: Crystal structure prediction and experiment, Earth Planet. Sci. Lett. **241**, 95 (2006).

[48] A. O. Lyakhov, A. R. Oganov, and M. Valle, How to predict very large and complex crystal structures, Comput. Phys. Commun. **181**, 1623 (2010).

[49] A. R. Oganov, A. O. Lyakhov, and M. Valle, How evolutionary crystal structure prediction works—and why, Acc. Chem. Res. **44**, 227 (2011).

[50] A. O. Lyakhov, A. R. Oganov, H. T. Stokes, and Q. Zhu, New developments in evolutionary structure predic-

tion algorithm uspex, Comput. Phys. Commun. **184**, 1172 (2013).

[51] J. Heyd, G. E. Scuseria, and M. Ernzerhof, Erratum: "Hybrid functionals based on a screened Coulomb potential" [J. Chem. Phys. 118, 8207 (2003)], J. Chem. Phys. **124**, 219906 (2006).

[52] G. Kresse and J. Hafner, *Ab initio* molecular dynamics for liquid metals, Phys. Rev. B **47**, 558 (1993).

[53] G. Kresse and J. Furthmüller, Efficient iterative schemes for *ab initio* total-energy calculations using a plane-wave basis set, Phys. Rev. B **54**, 11169 (1996).

[54] G. Kresse and D. Joubert, From ultrasoft pseudopotentials to the projector augmented-wave method, Phys. Rev. B **59**, 1758 (1999).

[55] J. P. Perdew, K. Burke, and M. Ernzerhof, Generalized gradient approximation made simple, Phys. Rev. Lett. **77**, 3865 (1996).

[56] H. J. Monkhorst and J. D. Pack, Special points for brillouin-zone integrations, Phys. Rev. B **13**, 5188 (1976).

[57] P. E. Blöchl, O. Jepsen, and O. K. Andersen, Improved tetrahedron method for brillouin-zone integrations, Phys. Rev. B **49**, 16223 (1994).

[58] X. Gonze, First-principles responses of solids to atomic displacements and homogeneous electric fields: Implementation of a conjugate-gradient algorithm, Phys. Rev. B **55**, 10337 (1997).

[59] X. Gonze, B. Amadon, P.-M. Anglade, J.-M. Beuken, F. Bottin, P. Boulanger, F. Bruneval, D. Caliste, R. Caracas, M. Cote, T. Deutsch, L. Genovese, Ph. Ghosez, M. Giantomassi, S. Goedecker, D.R. Hamann, P. Hermet, F. Jollet, G. Jomard, S. Leroux *et al.*, ABINIT: First-principles approach to material and nanosystem properties, Comput. Phys. Commun. **180**, 2582 (2009).

[60] See Supplemental Material at http://link.aps.org/supplemental/10.1103/PhysRevB.110.064106 for structural information, Raman shifts, DOS, phonon density, and distances analysis.

[61] M. Methfessel and A. T. Paxton, High-precision sampling for brillouin-zone integration in metals, Phys. Rev. B **40**, 3616 (1989).

[62] H. T. Stokes and D. M. Hatch, Findsym: program for identifying the space-group symmetry of a crystal, J. Appl. Crystallogr. **38**, 237 (2005).

[63] W. Kraus and G. Nolze, *POWDER CELL* – a program for the representation and manipulation of crystal structures and calculation of the resulting x-ray powder patterns, J. Appl. Crystallogr. **29**, 301 (1996).

[64] S. Nosé, A unified formulation of the constant temperature molecular dynamics methods, J. Chem. Phys. **81**, 511 (1984).

[65] W. G. Hoover, Canonical dynamics: Equilibrium phase-space distributions, Phys. Rev. A **31**, 1695 (1985).

[66] P. B. Allen and R. C. Dynes, Transition temperature of strong-coupled superconductors reanalyzed, Phys. Rev. B **12**, 905 (1975).

[67] P. Dalladay-Simpson, B. Monserrat, L. Zhang, and F. Gorelli, Distinct vibrational signatures and complex phase behavior in metallic oxygen, Matter Radiation Extr. **9**, 028401 (2024).